Supporting Information

Disentangling the Degradation Pathways of Highly Defective PtNi/C Nanostructures – An *Operando* Wide and Small Angle X-Ray Scattering Study

Tristan Asset,[*,†,‡,¶] Cedric J. Gommes,[‡] Jakub Drnec,[§] Pierre Bordet,[‖] Raphaël Chattot,[⊥,§] Isaac Martens,[#,@] Jaysen Nelayah,[△] Nathalie Job,[‡] Frédéric Maillard,[†] and Laëtitia Dubau[*,†]

†*Univ. Grenoble Alpes, CNRS, Grenoble-INP (Institute of Engineering Univ. Grenoble Alpes), Université Savoie-Mont-Blanc, LEPMI, 38000 Grenoble, France.*

‡*University of Liège, Department of Chemical Engineering - Nanomaterials, Catalysis, Electrochemistry, B6a, Sart-Tilman, B-4000 Liège, Belgium.*

¶*Center for Micro-Engineered Materials and Department of Chemical and Biological Engineering, University of New Mexico, Albuquerque, NM 87131, USA*

§*ESRF, ID 31 Beamline, BP 220, F-38043 Grenoble, France*

‖*CNRS, Institut Néel, F-38000 Grenoble, France*

⊥*Univ. Grenoble Alpes, CNRS, Grenoble-INP, Université Savoie-Mont-Blanc, LEPMI, 38000 Grenoble, France.*

#*AMPEL, The University of British Columbia, 2355 East Mall, Vancouver, BC V6T 1Z4, Canada*

@*Department of Chemistry, The University of British Columbia, 2036 Main Mall, Vancouver, BC V6T 1Z4, Canada*

△*Laboratoire Matériaux et Phénomènes Quantiques (MPQ), UMR 7162 CNRS & Université Paris-Diderot, Bâtiment Condorcet, 4 rue Elsa Morante, F-75205 Paris Cedex 13, France*

E-mail: tristanasset@gmail.com; laetitia.dubau@lepmi.grenoble-inp.fr

Contents

1 Synthesis of the Porous Hollow PtNi/C Nanoparticles

0.440 mmol of $Pt(NH_3)4Cl_2H_2O$ (Alfa Aesar Premion 99.995 % metal basis) and 1.32 mmol of $NiCl_2$ (Alfa Aesar anhydrous 99.99 % metal basis) were first dissolved in 140 mL of deionised water and 10 mL of ethanol in the presence of 0.3 g of dispersed Vulcan XC72 (Cabot). 23 wt. % was the target Pt content. An aqueous solution of sodium borohydride (Aldrich 99.99 %, 208 mg dissolved in 25 mL) was added at 5 mL min^{-1} while the solution was magnetically stirred at room temperature. After $t = 1$ h, the solution was filtered, the powder thoroughly washed with Milli-Q water and dried for $t = 45$ min at $T = 383$ K. The resulting powder was then acid leached under magnetic stirring in a 1 M H_2SO_4 solution at $T = 298 \pm 5$ K for $t = 22$ h, then filtered, washed and dried for $t = 45$ min at $T = 383$ K.

2 Transmission Electron Microscopy

The micrographs of the the PtNi/C powder scraped from the catalytic layers were obtained using the bright field imaging with a JEOL 2010 TEM operating at 200 kV with a point-to-point resolution of 0.19 nm. The particle size distribution of the porous hollow PtNi/C electrocatalysts was built from the TEM micrographs obtained at low/medium magnification ($\times$ 80,000 / $\times$ 150,000), using the Feret diameter. To obtain an accurate imaging of the atomic structure of nanoparticles, high-resolution TEM (HR-TEM) micrographs using a JEM-ARM 200F (JEOL) microscope equipped with a cold-field emission gun and an image aberration corrector (the operating voltage was 200 kV). The analysed electrocatalysts were deposited onto carbon-coated lacey copper or gold grids (Agar) after being scratched from the gas diffusion layer. A scanning transmission electron microscope (STEM, i.e. the electron beam is focused on a fine spot and scans over the selected area) was used to analyse the chemical composition of single NPs before and after AST in energy dispersive X-ray

(EDX) mode. The EDX mapping was obtained using a JEOL 2100F microscope operated at 200 kV and equipped with a retractable large angle silicon drift detector (Centurio). The quantitative analyses were performed on Pt L line and Ni K lines using the K factor provided by the JEOL software.

3 Atomic Absorption Spectroscopy

The Ni and Pt content of the fresh electrocatalyst was established by Atomic Absorption Spectroscopy (AAS - PinAACle 900F, PerkinElmer). The electrocatalyst (5 $\pm$ 1 mg) was first digested in aqua regia (HCl:HNO_3 3:1 volumic ratio) made from high-purity acids (37 vol. % ACS Reagent Sigma Aldrich and 65 vol. % Sigma-Aldrich) for $t = 72$ h at $T = 298 \pm 1$ K. The solution was then diluted sevenfold to reach the AAS range for Pt and Ni. The metals contents were then determined using three series of three measurements. The wavelengths considered for Pt and Ni were $\lambda = 266.0$ nm and $\lambda = 232.0$ nm, respectively.

4 X-Ray Diffraction

The X-ray diffraction patterns of the electrocatalyst before ageing were determined with a PANalytical X'Pert Pro MPD vertical goniometer/diffractometer with a diffracted-beam monochromator (Cu Kα radiation, $\lambda = 0.15406$ nm) operating at 45 kV and 40 mA. The 2θ range was 10 - 125° and the step size 0.033°.

5 Electrochemical Characterization in 4-Electrode Cell

The electrocatalyst suspensions were composed of (i) 10 mg of the electrocatalyst powder (for a Pt weight fraction of 20 wt. %), (ii) 54 μL of a Nafion® 5 wt. % solution (Sigma-Aldrich), *i.e.* 2.36 mg, therefore achieving an ionomer / carbon mass ratio of 0.3, (iii) 3600 μL of Milli-Q water and (iv) 1446 μL of isopropyl alcohol (99.5 % Acros Organics). The

electrocatalyst inks were first homogenised for $t = 20$ s using an ultrasonic probe and then placed $t = 15$ min in an ultrasonic bath. The catalytic inks were not used more than 2 weeks after their preparation, thus ensuring reproducible electrocatalytic measurements as described in Ref.[1] The uniformity and the homogeneity of the catalytic layer are pivotal for reproducible electrocatalytic measurements.[2,3] Therefore, 10 μL of the electrocatalyst suspension were deposited (targeting a loading of 20 μg of Pt per geometrical cm^2) on the working electrode while rotating at $\omega = 500$ rpm and drying under a heat flux. Prior to any electrochemical measurement, the fresh working electrode was immersed in the deaerated electrolyte at $E = 0.1$ V *vs.* RHE.

The electrochemical experiments were then performed in the following order:

(i) 50 cyclic voltammograms (CVs) between 0.05 and 1.23 V *vs.* RHE at a scan rate $v = 0.500$ V s^{-1};

(ii) 3 CVs between 0.05 and 1.23 V *vs.* RHE at $v = 0.020$ V s^{-1};

(iii) the CO_{ads} stripping in which the CO was bubbled in the electrolytic solution for $t = 6$ min followed by a purge of the solution by Ar during $t = 29$ min at $E = 0.1$ V *vs.* RHE and the recording of 3 CVs at $v = 0.02$ V s^{-1} between 0.05 and 1.23 V *vs.* RHE;

(iv) 6 linear sweep voltammograms (LSVs) from 0.20 to 1.05 V *vs.* RHE in O_2-saturated electrolytic solution at $v = 0.005$ V s^{-1} and at different revolution rates ($\omega = 400$, 900, 1600 and 2500 rotation per minutes - rpm) to determine the electrocatalytic activity of the thin-film electrodes for the ORR.

6 Operando Cell

Operando WAXS and SAXS measurements were performed at the ID31 beamline of the European Synchrotron Radiation Facility (ESRF) in Grenoble, France, to investigate the degradation mechanisms of porous hollow PtNi/C NPs. A home-made cell (see Figure S1

and Napporn et al.[4]), made of Kel-F (homopolymer of chlorotrifluoroethylene), was used to characterize a gas-diffusion electrode (GDE), *i.e.* a commercial GDL (Sigracet 25BC, SGL Carbon) coated with a suspension of porous hollow PtNi/C ink, and hot-pressed on a Nafion® membrane (N115, Ionpower). The theoretical Pt loading was 250 μgPt cm^{-2}_{geo}. The cell was designed to minimize the thickness of the electrolyte layer on the beam path. The GDE was connected to the potentiostat by a circular gold current collector (WE). The counter electrode was a circular Pt wire (CE) and the reference was a commercial RHE (Hydroflex, Gaskatel GmbH) connected to a Pt wire (used to avoid any low-frequency disturbance of the electrochemical measurements). The current collector and the CE were maintained out of the beam trajectory. For more information on the cell geometry and composition, please refer to Figure S1.

The electrocatalysts were aged by a load-cycle protocol during 5,000 cycles between 0.6 and 1.0 V *vs.* RHE or 1.1 V *vs.* RHE at $v = 0.050$ V s^{-1} after 5 cycles at $v = 0.020$ V s^{-1} between 0.10 V and 1.23 V *vs.* RHE at a targeted temperature $T_{theo} = 353$ K (a loss of *ca.* 10 - 20 K was assumed during the circulation of the electrolyte from the thermostatic bath to the electrochemical cell). All experiments were conducted in argon-purged electrolyte.

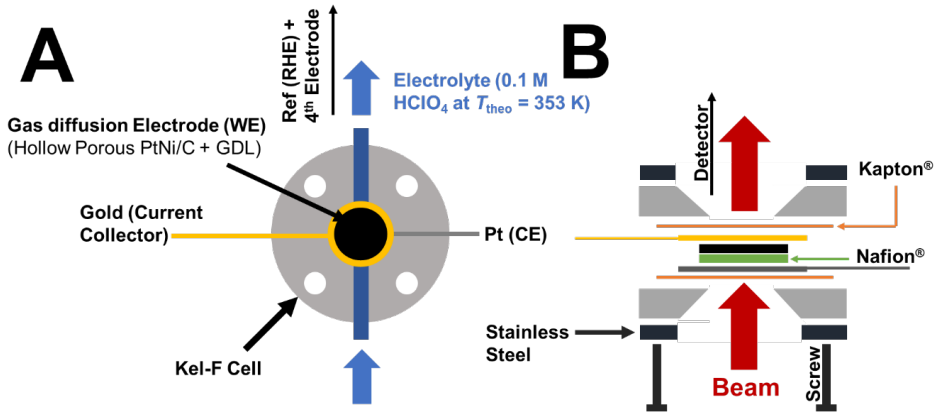

Figure S1: Scheme of the electrochemical cell used to investigate the ageing mechanisms of porous hollow PtNi/C NPs by *operando* WAXS and SAXS measurements: (A) front and (B) side views.

7 Wide Angle X-Ray Scattering and Rietveld Refinement

The X-ray beam was focused with two transfocators to a size of 4 μm $\times$ 30 μm (vertical $\times$ horizontal) at the sample position, with a flux of 10^{12} photons s^{-1}. The scattered signal was collected with Dectris Pilatus CdTe 2M detector positioned 300 mm behind the sample. The energy, detector distance and tilts were calibrated using a standard CeO_2 powder and the 2D diffraction patterns were reduced to 1D curves using pyFAI software package.[5] During the catalyst ageing, one WAXS pattern was measured every 20 min, with an acquisition time of t =10 s. All experiments were conducted in argon-purged electrolyte.

The Rietveld refinements were carried out for 2θ between 3° and 20° using the Fullprof software, considering the Fm-3m structure of a cubic closed-packed metal ($a \sim 3.9$ Å). The instrumental resolution function was determined by the refinement of the CeO_2 standard sample. The Thomson-Cox-Hastings profile function was adopted with possibility for uniaxial anisotropic broadening from size origin.

8 Small Angle X-Ray Scattering

The scattered signal was collected with Dexela 2923 positioned 6 m behind the sample. A long flight tube inserted between the detector and the sample was used to limit the air scattering of the direct beam. The beam stop was positioned at the end of the flight tube, about 150 mm from the detector. The size of the beam at the sample position was 4 μm $\times$ 30 μm (vertical $\times$ horizontal). The energy, detector distance and tilts were calibrated using a standard Ag behenate powder and the 2D diffraction patterns were reduced to 1D curves using pyFAI software package.[5] During the catalyst ageing, one SAXS pattern was measured every 20 min, with an acquisition time of t =10 s. All experiments were conducted in argon-purged electrolyte.

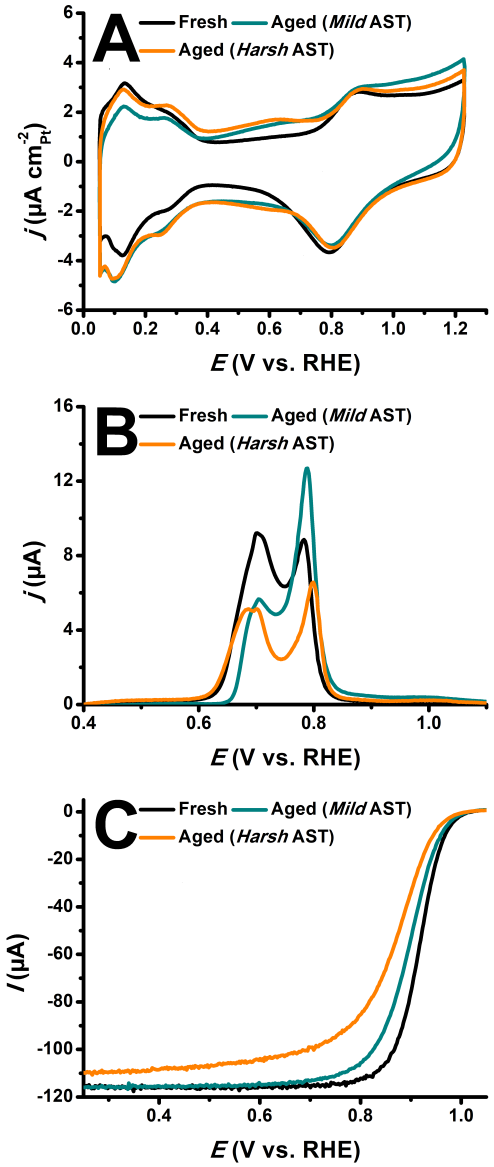

Figure S2: Electrocatalytic properties of the porous hollow PtNi/C electrocatalyst before and after *ex-situ* mild and harsh AST. (A) Cyclic voltammograms in N_2-saturated 0.1 M $HClO_4$ (v = 0.020 V s^{-1}); (B) CO Stripping in N_2-saturated 0.1 M $HClO_4$ (v = 0.020 V s^{-1}); (C) Linear sweep voltammograms in O_2-saturated 0.1 M $HClO_4$ in Tafel representation, corrected from the Ohmic drop (v = 0.005 V s^{-1}, ω = 1600 rpm).

Table S1: Physical, chemical and electrochemical properties of the porous hollow PtNi/C electrocatalyst used in the *operando* WAXS and SAXS measurements.

	Fresh	Aged 0.6 - 1.0 V *vs.* RHE	Aged 0.6 - 1.1 V *vs.* RHE	
Pt (wt. %)	20.3 ± 0.5	n.a.	n.a.	
Ni_{AAS} (at. %)	20 ± 0.5	n.a.	n.a.	
a_{Pt-Pt} (nm)	0.389 ± 0.001	n.a.	n.a.	
d_{XRD} (nm)	2.4 ± 0.1	n.a.	n.a.	
Ni_{X-EDS} (at. %)	9.8 ± 0.8	6.7 ± 0.7	7.3 ± 0.6	3.9 ± 0.9
d_{ext} (nm)	10.9 ± 2.5	11.1 ± 2.6	11.9 ± 2.7	7.3 ± 2.1
d_{in} (nm)	6.2 ± 1.8	6.2 ± 2.2	5.9 ± 1.9	0
$S_{Pt,CO}$ ($m^2\ g_{Pt}^{-1}$)	42.6 ± 5	31.6	24.5	
$SA_{0.95}$ ($\mu A\ cm_{Pt}^{-2}$)	154 ± 14	129	92	
$SA_{0.90}$ ($\mu A\ cm_{Pt}^{-2}$)	1287 ± 63	816	536	
$MA_{0.95}$ ($\mu A\ cm_{Pt}^{-2}$)	65.5 ± 1	40	23	
$MA_{0.90}$ ($\mu A\ cm_{Pt}^{-2}$)	546 ± 30	259	134	

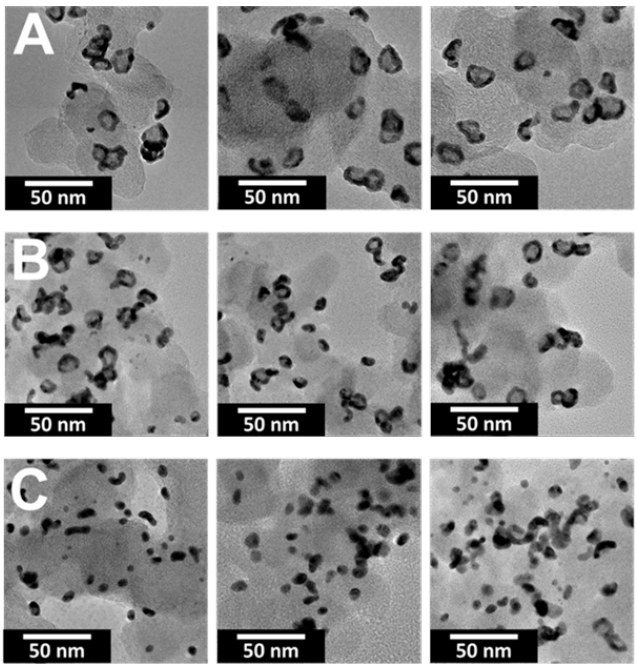

Figure S3: TEM micrographs of the gas diffusion electrode (GDE) (A) before and after 5,000 cycles in Ar-saturated 0.1 M $HClO_4$ between 0.6 and (B) 1.0 V *vs.* RHE or (C) 1.1 V *vs.* RHE. Other conditions: $v = 0.050$ V s^{-1} and $T = 353 \pm 1$ K.

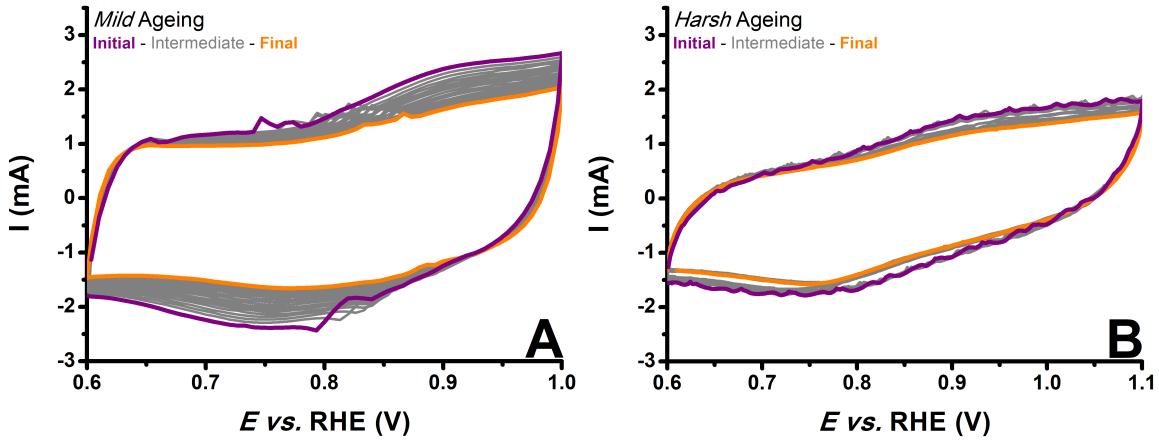

Figure S4: Evolution of the electrochemical signal during the *operando* (A) mild & (B) harsh ageing of the porous hollow PtNi/C, in N_2-saturated 0.1 M $HClO_4$ (v =0.050 V s^{-1}). The differences in the signal initial shape were ascribed to slight change in the cell resistance in-between experiments. .

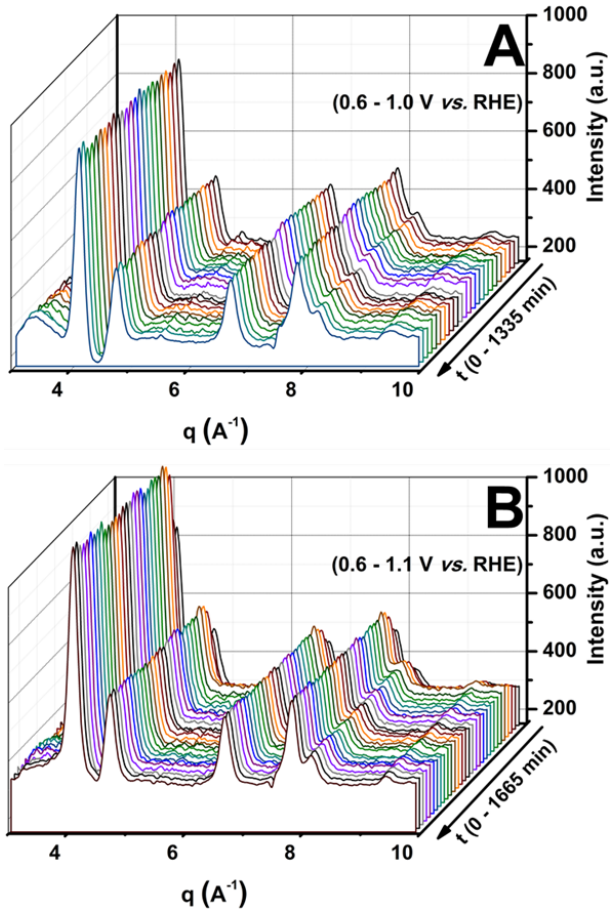

Figure S5: Variations of the WAXS patterns recorded onto a porous hollow PtNi/C electrocatalyst during 5,000 cycles in Ar-saturated 0.1 M $HClO_4$ between (A) 0.6 and 1.0 V *vs.* RHE or (B) 1.1 V *vs.* RHE ($v = 0.050$ V s^{-1} and $T = 353 \pm 1$ K).

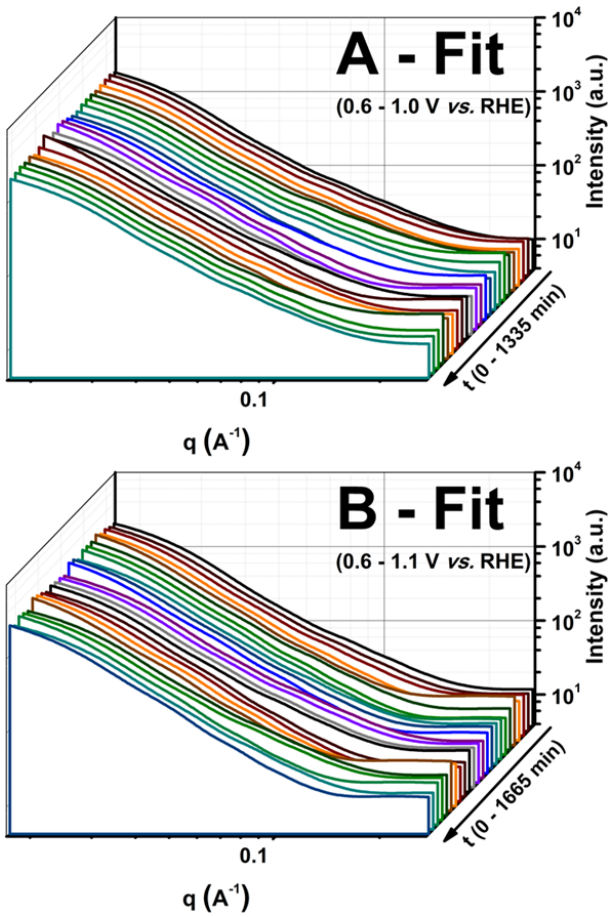

Figure S6: Variations of the fitted SAXS patterns recorded onto a porous hollow PtNi/C electrocatalyst during 5,000 cycles in Ar-saturated 0.1 M $HClO_4$ between (A) 0.6 and 1.0 V *vs.* RHE or (B) 1.1 V *vs.* RHE ($v = 0.050$ V s^{-1} and $T = 353 \pm 1$ K).

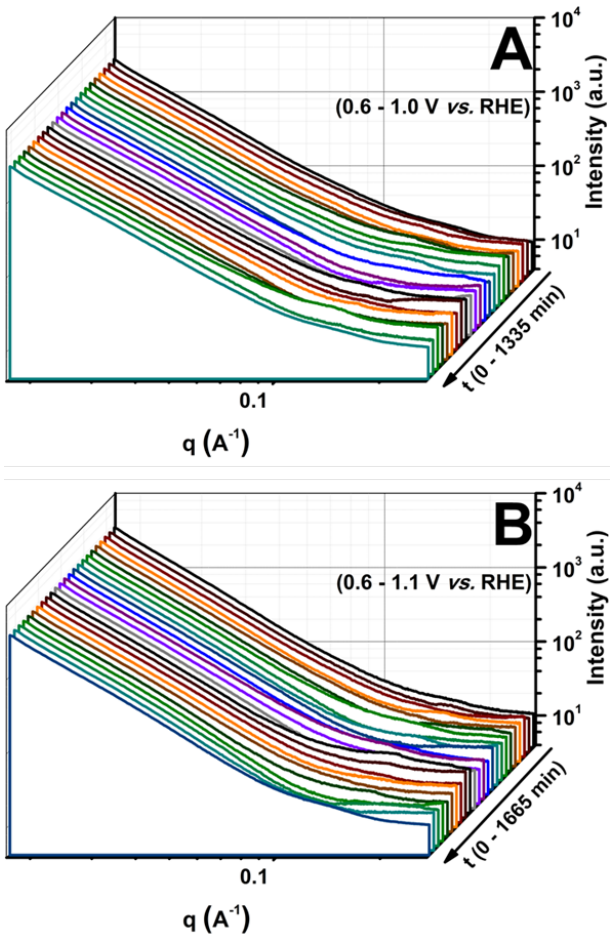

Figure S7: Variations of the non-fitted SAXS patterns recorded onto a porous hollow PtNi/C electrocatalyst during 5,000 cycles in Ar-saturated 0.1 M $HClO_4$ between (A) 0.6 and 1.0 V *vs.* RHE or (B) 1.1 V *vs.* RHE ($v = 0.050$ V s^{-1} and $T = 353 \pm 1$ K).

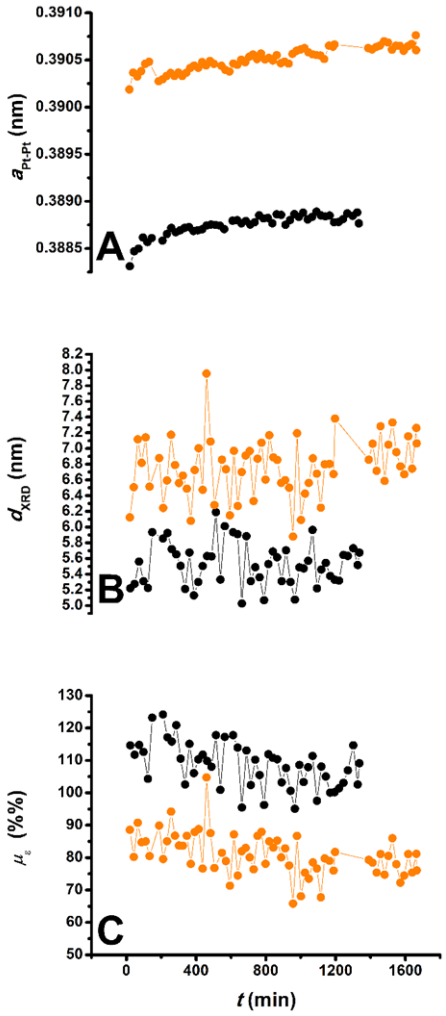

Figure S8: Variations of structural parameters extracted from Rietveld refinement of XRD patterns measured on porous hollow PtNi/C electrocatalyst during 5 000 potential cycles in Ar-saturated 0.1 M $HClO_4$ between 0.6 and 1.0 V *vs.* RHE or 1.1 V *vs.* RHE (v = 0.050 V s^{-1} and T = 353 ± 1 K). (A) Variation of the lattice parameter a_{Pt-Pt}, (B) variation of the average crystallite size, d_{XRD} and (C) variation of the microstrain μ_ϵ. Since the number of potential cycles was kept constant, the AST between 0.6 and 1.1 V *vs.* RHE was 20% longer than the AST between 0.6 and 1.0 V *vs.* RHE.

9 Small-Angle Scattering Data Analysis

A general data analysis procedure for analyzing the small-angle scattering by a porous solid, with material loaded in the pores is described in Ref.[6] We particularize here this approach to the case of hollow nanoparticles supported on carbon.

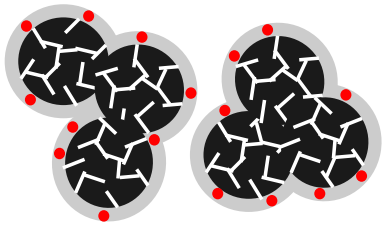

Figure S9: Sketch of the general type of structure assumed for the SAXS data analysis. The nanoparticles (red) are positioned randomly within a geometrical layer (grey) that covers the surface the of the porous material (black).

The specific model we assume in the present analysis is sketched in Fig. S9. The carbon support is shown in black, and the smaller white features in the figure symbolise the micropores that are inaccessible to the nanoparticles. The nanoparticles are randomly positioned at the surface of the mesopores. The mathematical model is constructed in two steps: first by defining a thin geometrical layer covering the mesopore surface (grey in figure), and then by distributing randomly the nanoparticles (red in the figure) within that layer. The particles themselves are modelled as hollow spheres with their shells having the same electron density as Pt. The polydispersity of the particles is modelled by assuming that all particles have the same shell thickness, but that their inner radii are distributed according to a statistical gamma distribution. The gamma distribution has two parameters - the average value and the shape parameter k - and it contains a narrow Gaussian-like and the exponential distributions as particular cases, for large and small values of k respectively.

The structure of the present section is the following

(i) In section 9.1, we derive the general equation that relates the complete SAXS signal to the various structural levels in the model: the porous support, the layer where the

particles are positioned, and the particles themselves. The central result is Eq. (S5);

(ii) In the following sections (9.2.1, 9.2.2, 9.2.3 and 9.2.4), the various contributions to Eq. (S5) are modelled explicitly. These developments build on the observation that the mesopores are much larger than the particles themselves, which enables one to use a Debye-Bueche form factor for the solid (as well as for the layer, and for the solid-layer cross-correlations) without limiting the generality of the analysis. The form factor of the particles is described in detail in section 9.2.2;

(iii) In section 9.3, we describe how the model is practically used to fit the data. The solid support is fitted once and for all, based on ex-situ scattering data. For the operando SAXS, the support is assumed to remain unchanged as well as the overall metal loading. The only structural parameters used for the fit are the thickness of the nanoparticles shell e and the two parameters of the gamma distribution, namely the average inner radius $\langle R_I \rangle$ and the shape parameter k.

9.1 General Structural Model

The SAXS intensity $I(q)$ is the Fourier transform of the centred covariance of the electron density $\rho(\mathbf{x})$, defined as the number of electrons in a small volume of material centred on point $\mathbf{x}$. That is[7,8]

$$I(q) = \int_0^\infty \bar{C}_\rho(r) \frac{\sin(qr)}{qr} 4\pi r^2 \mathrm{d}r \tag{S1}$$

where the centred covariance is defined as

$$\bar{C}_\rho(r) = \langle \rho(\mathbf{x}) \rho(\mathbf{x}+\mathbf{r}) \rangle - \langle \rho(\mathbf{x}) \rangle^2 \tag{S2}$$

where the brackets $\langle\rangle$ stand for the average value calculated over all possible values of $\mathbf{x}$.

The general structural model assumed to analyze the SAXS data is sketched in Fig. S9. The scattering by such a structure is calculated using the general methods developed in.[6] In

particular the electron density of the structure is described as

$$\rho(\mathbf{x}) = \rho_S \mathcal{I}_S(\mathbf{x}) + \rho_P \mathcal{I}_L(\mathbf{x}) \mathcal{I}_P(\mathbf{x}) \tag{S3}$$

where $\mathcal{I}_S(\mathbf{x})$ is the indicator function of the solid, taking the value 1 is point $\mathbf{x}$ belongs to the solid and 0 otherwise, $\mathcal{I}_L$ is defined similarly for the layer that covers the solid surface. The indicator function of the particles $\mathcal{I}_P(\mathbf{x})$ is defined as if the particles were randomly distributed over the entire volume; it is the multiplication of $\mathcal{I}_P$ by $\mathcal{I}_L$ in Eq. (S3) that limits the particles to the surface of the solid.[6] The electron densities ρ_S and ρ_P are the relevant values of the materials that make up the solid and the particles.

Using the particular model in Eq. (S3) for the electron density, Eq. (S2) leads to the following expression for the covariance

$$\begin{aligned} \langle \rho(\mathbf{x}) \rho(\mathbf{x}+\mathbf{r}) \rangle &= \rho_S^2 \langle \mathcal{I}_S(\mathbf{x}) \mathcal{I}_S(\mathbf{x}+\mathbf{r}) \rangle \\ &+ \rho_P^2 \langle \mathcal{I}_L(\mathbf{x}) \mathcal{I}_L(\mathbf{x}+\mathbf{r}) \rangle \langle \mathcal{I}_P(\mathbf{x}) \mathcal{I}_P(\mathbf{x}+\mathbf{r}) \rangle \\ &+ 2\rho_S \rho_P \langle \mathcal{I}_M(\mathbf{x}) \rangle \langle \mathcal{I}_S(\mathbf{x}) \mathcal{I}_L(\mathbf{x}+\mathbf{r}) \rangle \end{aligned} \tag{S4}$$

where the brackets $\langle\rangle$ have the save meaning as in Eq. (S2). This can be written as follows in terms of the centred covariance

$$\begin{aligned} \bar{C}_\rho(r) &= \rho_S^2 \bar{C}_S(r) + \rho_P^2 (\bar{C}_L(r) + \phi_L^2) \bar{C}_P(r) \\ &\quad \rho_P^2 \phi_P^2 \bar{C}_L(r) + 2\rho_S \rho_P \phi_P \bar{C}_{SL}(r) \end{aligned} \tag{S5}$$

where we have used the general notation

$$\bar{C}_{XY} = \langle \mathcal{I}_X(\mathbf{x}) \mathcal{I}_Y(\mathbf{x}+\mathbf{r}) \rangle - \phi_X \phi_Y \tag{S6}$$

for the centred covariances of the various phases X and Y, and

$$\phi_X = \langle \mathcal{I}_X(\mathbf{x}) \rangle \tag{S7}$$

for the volume fraction of phase X.

9.2 Specific Functions Assumed

The scattered intensity is obtained as the Fourier transform of Eq. (S5), which contains four different contributions. They are detailed in the following four sections

9.2.1 Scattering Contribution from the Solid

The contribution of the solid itself $I_S(q)$ to the SAXS intensity is obtained at the Fourier transform of the term proportional to $\bar{C}_S(r)$ in Eq. (S5). We model it as

$$I_S(q) = \rho_S^2 \left[\phi_S(1-\phi_S) \frac{8\pi l_S^3}{(1+(ql_S)^2)^2} + \frac{\alpha}{q^2} \right] \tag{S8}$$

The first term is a Debye-Bueche form factor[9] that accounts for the scattering by the mesoscale structure of the carbon where ϕ_S is the volume fraction of solid (porosity equal to $1-\phi_S$) and l_S is a characteristic length that characterizes both the solid skeleton and the pores. The second term in Eq. (S8) accounts for the Angstrom-scale electron density fluctuations within the carbon. This type of q^{-2} scattering is observed for a wide variety of carbon material,[10–12] and it proves necessary here as well.

Because the Debye-Bueche formfactor is equivalent to an exponential covariance $\bar{C}_S(r) = \phi_S(1-\phi_S)\exp(-r/l_S)$ the length l_S is related to the surface area a_S by (see e.g.[13])

$$l_S = 4\frac{\phi_S(1-\phi_S)}{a_S} \tag{S9}$$

Nitrogen adsorption on the porous support measured independently from the SAXS provides

the porous volume is 0.39 cm^3/g. Assuming a skeletal density $\bar{\rho}_S = 2$ g/cm^3 for dense carbon, this value converts to $1 - \phi_S \simeq 0.44$. Nitrogen adsorption also provides a specific surface area S_m =150 m^2/g for the mesopores, which converts to

$$a_S \simeq 1.35\ 10^{-2} \mathring{A}^{-1} \tag{S10}$$

This value also assumes a density $\bar{\rho}_S = 2$ g/cm^3.

For further purposes, it is also useful to calculate the electron density ρ_S of the carbon. Assuming pure carbon, with a molar mass of $M = 12$ g, a number of 6 electrons per atom (or 6 Faradays per mole), and a specific mass of $\bar{\rho}_S = 2$ $g.cm^{-3}$, the estimated electron density is $\rho_S \simeq 1$ $F.cm^{-3}$.

9.2.2 Scattering Contribution from the Nanoparticles

The second contribution in Eq. (S5), proportional to $\bar{C}_P(r)$, describes the scattering by the nanoparticles themselves. That term can be simplified by noting that[6,14]

$$(\bar{C}_L(r) + \phi_L^2)\bar{C}_P(r) \simeq \phi_L \bar{C}_P(r) \tag{S11}$$

because the layer is much more extended (at least laterally) than the particles themselves, so that $\bar{C}_P(r)$ decreases to 0 faster than $\bar{C}_L(r)$.

If we assume that the particles are randomly distributed with respect to one another, the covariance of the particles can be expressed as

$$\bar{C}_P(r) = \theta_P \bar{K}_P(r) \tag{S12}$$

where θ_P is the number of particles per unit volume of the layer, and $\bar{K}_P(r)$ is the normalized geometrical covariogram of the particles ($\bar{K}_P(r) = K_P(r)/\langle V^2 \rangle$, where $\langle V^2 \rangle$ is the average squared volume of the particle). Because the Fourier transform of $\bar{K}_P(r)$ is the particle form

factor $P(q)$ (normalised so that $P(0) = 1$), the final expression for the particle scattering is

$$I_P(q) = \phi_L \rho_P^2 \theta \langle V^2 \rangle P(q) \tag{S13}$$

This is the usual expression for the scattering of non-interacting nanoparticles,[15] which is multiplied here by ϕ_L because this is the fraction of the material volume where this structure is found.

For further purposes, it is convenient to rewrite this as a function of $\phi_P = \theta_P \langle V \rangle$ as

$$I_P(q) = \phi_L \rho_P^2 \phi_P \bar{P}(q) \tag{S14}$$

with

$$\bar{P}(q) = \frac{\langle V^2 \rangle}{\langle V \rangle} P(q) \tag{S15}$$

The form factors $P(q)$ and $\bar{P}(q)$ are normalised such that $P(\to 0) = 1$ and $\bar{P}(\to 0) = \langle V^2 \rangle / \langle V \rangle$.

The form factor of a spherical shell, with inner and outer radii R_I and R_O is calculated as[15]

$$\bar{P}(q) = \frac{(V_O F(R_O q) - V_I F(R_I q))^2}{V_O - V_I} \tag{S16}$$

with

$$F(x) = 3 \frac{\sin(x) - x \cos(x)}{x^3} \tag{S17}$$

and $V_{O/I} = (4/3)\pi R_{O/I}^3$.

For the fitting of the SAXS data polydispersed hollow spherical particles are considered, with the inner radius R_I distributed according to a gamma distribution with size parameter $\langle R_I \rangle$ (average inner radius) and shape parameter k (standard deviation $\sigma_{RI} = \langle R_I \rangle / \sqrt{k}$. The thickness e (from the French word *épaisseur*) of the shell is assumed to be a constant,

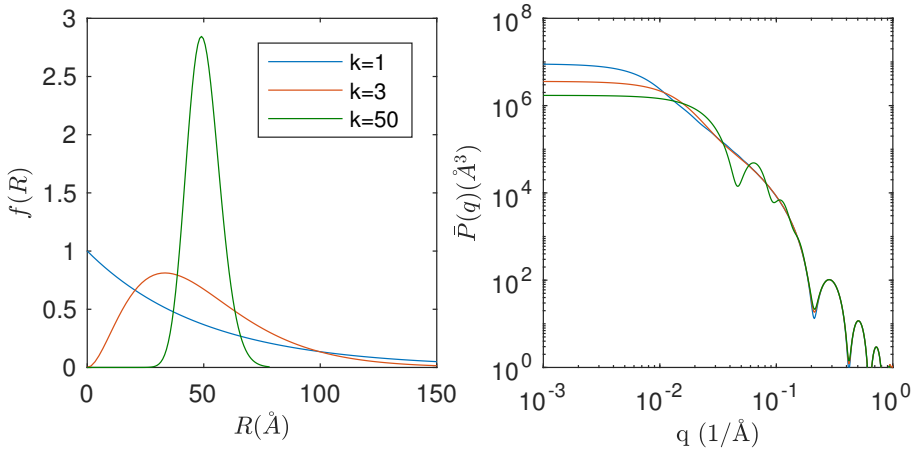

Figure S10: Left: gamma distributions with average value $\langle R_I \rangle = 50 Å$ and shape parameter $k = 1$, $k = 3$ and $k = 50$. Right: corresponding form factors $\bar{P}(q)$ assuming a shell thickness $e = 30$ Å.

independent of the inner radius.

$$\bar{P}(q) = \frac{1}{\langle V \rangle} \int_0^\infty f(R_I) \left[\frac{4\pi(R_I + e)^3}{3} F(q(R_I + e)) - \frac{4\pi R_I^3}{3} F(qR_I) \right]^2 \mathrm{d}R_I \tag{S18}$$

where

$$\langle V \rangle = \int_0^\infty f(R_I) \left[\frac{4\pi(R_I + e)^3}{3} - \frac{4\pi R_I^3}{3} \right] \mathrm{d}R_I \tag{S19}$$

is the average volume of the shell. The distributions and corresponding form factors are illustrated in Fig. S10.

For further purposes, it is also useful to calculate the electron density ρ_P of the particles. Assuming pure platinum, with a molar mass of $M = 195$ g, a number of 78 electrons per atom (or 78 Faradays per mole), and a specific mass of $\bar{\rho}_P = 21.45$ g.cm^{-3}, the estimated electron density is $\rho_P \simeq 8.6$ F.cm^{-3}.

9.2.3 Scattering Contribution from the Layer

The Fourier transform of the third term in Eq. (S5), proportional to $\bar{C}_L(r)$, is the contribution of the layer to the scattering pattern. We refer to that contribution as $I_L(q)$.

The exact form of the function $C_L(r)$ is unknown. However, it is a function that decreases from the value $C_L(0) = \phi_L$ to $C_L(\infty) = \phi_L^2$, with initial slope equal to $a_L/4$ where a_L is the specific surface area of the layer. Assuming that the layer is thin its specific surface area is approximately $2 \times a_S$, because half of the layer surface is in contact with the solid (area a_S) and the other half (area a_S) is free. A convenient function that satisfies these conditions is therefore

$$C_L(r) = \phi_L(1 - \phi_L)\exp(-r/l_L) + \phi_L^2 \tag{S20}$$

with

$$l_L = \frac{2\phi_L(1 - \phi_L)}{a_S} = 2\delta(1 - a_S\delta) \tag{S21}$$

where the second equality results from expressing $\phi_L = a_S\delta$, with δ being the thickness of the layer.

After Fourier transformation, one obtains

$$I_L(q) = [\rho_P\phi_P]^2\,\phi_L(1 - \phi_L)\frac{8\pi l_L^3}{(1 + (ql_L)^2)^2} \tag{S22}$$

Note that the only extra parameter that enters $I_L(q)$, compared to $I_S(q)$ and $I_P(q)$ is the layer thickness δ, from which ϕ_L and l_L are calculated.

9.2.4 Scattering Contribution from the Solid-Layer Cross-Correlation

The Fourier transform of the fourth and last term in Eq. (S5), proportional to $\bar{C}_{SL}(r)$, is the cross-contribution of the layer and the solid to the scattering pattern. We refer to that contribution as $I_{SL}(q)$.

To evaluate $I_{SL}(q)$ one has to know the cross-covariance $C_{SL}(r)$. This is a function that starts from $C_{SL}(0) = 0$ to $C_{SL}(\infty) = \phi_L\phi_S$ with initial slope equal to $a_{SL}/4$, where a_{SL} is the specific surface area of the S/L interface. The contact area between the layer and the

solid is simply a_S. A function that satisfies these conditions is

$$C_{SL}(r) = \phi_S \phi_L \left(1 - \exp(-r/l_{SL})\right) \tag{S23}$$

with

$$l_{SL} = \frac{4\phi_S \phi_L}{a_S} = 4\phi_S \delta \tag{S24}$$

where the second equality results from expressing $\phi_L = a_S \delta$. After Fourier transformation, the second contribution on the first line of Eq. (S5) is

$$I_{SL}(q) = -2\rho_S \left[\rho_P \phi_P\right] \phi_S \phi_L \frac{8\pi l_{SL}^3}{(1 + (q l_{SL})^2)^2} \tag{S25}$$

No additional parameter enters this equation, compared to $I_L(q)$ and $I_S(q)$.

9.3 Least-Square Fitting of the Data

Putting together all contributions to the scattering (Eqs. S8, S14, S22, S25) the following expression is obtained

$$\begin{aligned} I_{model}(q) &= \rho_S^2 \left[\phi_m(1-\phi_m)\frac{8\pi l_m^3}{(1+(q l_m)^2)^2} + \frac{\alpha}{q^2}\right] \\ &- 2\rho_S \left[\rho_P \phi_P\right] \phi_S \phi_L \frac{8\pi l_{SL}^3}{(1+(q l_{SL})^2)^2} \\ &+ \left[\rho_P \phi_P\right]^2 \phi_L (1-\phi_L) \frac{8\pi l_L^3}{(1+(q l_L)^2)^2} \\ &+ \phi_L \rho_P^2 \phi_P \bar{P}(q) \end{aligned} \tag{S26}$$

9.3.1 Solid Support

The particular case of the solid support is obtained from Eq. (S26) by setting $\phi_P = 0$. The model that is fitted to the data is

$$I_{model}(q) = A \left\{ \phi_S(1-\phi_S) \frac{8\pi l_S^3}{(1+(q l_S)^2)^2} + \frac{\alpha}{q^2} \right\} \tag{S27}$$

where the factor A account for the overall presence of the porous material in the beam. The other fitting parameters are ϕ_S, l_S, and α. The values of ϕ_S and l_S were allowed to vary only by $\pm$ 30 % compared to the starting values derived from nitrogen adsorption (see Sec. 9.2.1).

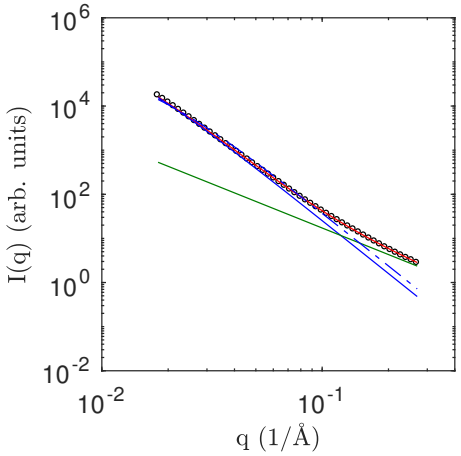

Figure S11: SAXS pattern of the XC72 porous support ($\circ$) together with the best fit using Eq. (S27) (red line). The blue and green lines are the mesoscale and microscale contributions. The dashed blue line was obtained from the values of parameters l_S and ϕ_S derived from nitrogen adsorption (with no fitting).

The best fit is illustrated in Fig. S11. The values of the fitted parameters are : $\phi_S = 0.5$ (initial value, $\phi_S = 0.56$ from nitrogen adsorption), $l_S = 111$ Å (initial value $l_S = 71$ Å from nitrogen adsorption) and $\alpha = 3.8$.

9.3.2 Supported Nanoparticles

To analyze the *operando* SAXS data all the contributions in Eq. (S26) have to be considered. The fitted model is the following

$$I_{data}(q) = A \times I_{model}(q, \beta_S, \beta_P) + B \tag{S28}$$

where A has the same meaning as in Eq. (S27) and and B is a flat background contribution that is required to account for the liquid scattering. The parameters of the model are grouped

symbolically into β_S and β_P, corresponding to those that characterize support (ϕ_S, l_S, α) and those of the nanoparticles ($\langle R_I \rangle$, e and k).

For fitting the *operando* SAXS data, only the parameters of the nanoparticles β_P as well as A and B were adjusted. All other quantities that enter Eq. (S26) were set to the following values

(i) The parameters of the support ϕ_S, l_S (equivalent to a_S via Eq. (S9)) and α were fixed to the values obtained from the analysis of the empty support;

(ii) The thickness δ of the layer L in which nanoparticles are found is set to $\delta = 100$ Å. This corresponds to an a-priori diameter of the particles. From that values, the volume fraction of the layer is estimated as $\phi_L = a_S \delta$ and the length scales l_L and l_{SL} are obtained from Eqs. (S21) and (S24);

(iii) The electron densities were set to $\rho_S \simeq 0.5$ F/cm^3 and $\rho_P \simeq 8.1$ F/cm^3. These values correspond to the densities calculated in Secs. 9.2.1 and 9.2.2, from which the electron density of water (0.5 F/cm^3) was subtracted. This subtraction is necessary because the relevant contrast for the *operando* measurement is with respect to water, not to vacuum;

(iv) The volume fraction of the particles ϕ_P (within the layer) is calculated from the particle loading $\Lambda_P = 0.2$ grams of platinum per gram of carbon, via

$$\phi_P = \frac{1}{\Lambda_P} \frac{\phi_L \bar{\rho}_P}{\phi_S \bar{\rho}_S} \tag{S29}$$

where $\bar{\rho}_S = 2$ g.cm^{-3} and $\bar{\rho}_P = 21.45$ g.cm^{-3} are the specific masses of the carbon and of the particles.

An example of fitting is provided in Fig. S12.

From the fitted parameters $\langle R_I \rangle$, k of the particle inner radius distribution as well as the

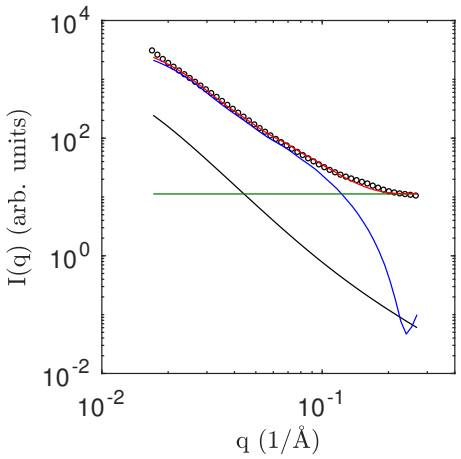

Figure S12: Example of *operando* SAXS data (first frame of the short-cycling run, ∘, see also Fig. S6) together with its best fit (red line), the total contribution of the support ($I_S + I_{SL} + I_L$, black), the nanoparticle contribution (blue), and the liquid background contribution (green).

thickness e of the shell, the specific surface area of the particles is calculated as follows

$$a_P = \frac{1}{\bar{\rho}_P \langle V \rangle} \int_0^\infty f(R_I) \left[4\pi R_I^2 + 4\pi (R_I + e)^2 \right] \, \mathrm{d}R_I \tag{S30}$$

where $f()$ is a gamma distribution with average $\langle R_I \rangle$ and shape parameter k, $\langle V \rangle$ is the average volume of the shell calculated as in Eq. (S19), and $\bar{\rho}_P \simeq 21.45$ g.cm^{-3} is the density of platinum.

10 χ^2-Test for the Time Evolution of Structural Parameters

The time-dependence of the structural parameters derived from WAXS and SAXS patterns are noisy. It is therefore necessary to determine which features of these time series are statistically significant before any physicochemical conclusion can be drawn from them. The statistical method used to obtain the continuous curves overlaid with the fitted parameters in Fig. 3 of the main text is a χ^2-test, as we explain now.

The structural parameters derived from the SAXS and WAXS are the lattice spacing a_{Pt-Pt}, the microstrain μ_ϵ, the crystallite size d_{XRD}, the inner and outer diameters d_{in} and d_{ext}, the geometrical area S_{Pt} of the hollow nanoparticles, as well as the shape parameter k of the gamma distribution of the inner diameters. All the quantities are statistically analyzed in the same manner, and we refer hereafter to any of them simply as y.

We consider three possible models to describe the time-dependence of y. The simplest consists in assuming that y is a constant, which does not evolve with time

$$y^{(1)}(t) = a_1 \tag{S31}$$

where a_1 is the only parameter of the model. In statistical terms, this model has one degree of freedom $\nu = 1$. The second model assumes a linear dependence

$$y^{(2)}(t) = a_1 + a_2 t \tag{S32}$$

which has two parameters ($\nu = 2$). The third model assumes an initial linear dependence, followed by a plateau

$$y^{(3)}(t) = \begin{cases} a_1 + a_2 t & \text{for} \quad t < a_3 \\ a_1 + a_2 a_3 & \text{for} \quad t \geq a_3 \end{cases} \tag{S33}$$

which has three parameters ($\nu = 3$), the third of which a_3 is the time beyond which y remains constant. The parameters of all the models are obtained via the minimisation of

$$\chi^2 = \sum_{i=1}^{N} \left[y_i - y^{(\nu)}(t_i) \right]^2 \tag{S34}$$

In the case of the third-order model $y^{(3)}$ the non-linear minimization is performed via the simplex methods.

The principle of our statistical analysis consists in testing successively the models against the data, in order of increasing complexity (from $\nu = 1$ to $\nu = 3$), and in keeping the first model that cannot be rejected based on a χ^2 test with a p-value of 0.9.[16] Because the variance of the error σ^2 on the individual data points is not known, we estimate it through the deviations between the measured values y_i and the third-order model, namely

$$\sigma^2 = \sum_{i=1}^{N} \frac{\left[y_i - y^{(3)}(t_i) \right]^2}{N - 3} \tag{S35}$$

where y_i is the structural parameter of interest (a_{Pt-Pt}, μ_ϵ, d_{XRD}, k, d_{ext}, d_{in}, or S_{Pt}) measured at time t_i, $y^{(3)}(t_i)$ is the value obtained through the three-parameter model, N is the number of data points, and $N - 3$ is the number of data point minus the number of parameters of the model. The p-values of all the fits (for $\nu = 1$ to $\nu = 3$) are then obtained in the usual way, as

$$p = \text{gammainc}\left(\frac{1}{2} \frac{\chi^2}{\sigma^2}, \frac{\nu}{2} \right) \tag{S36}$$

where gammainc() is the incomplete gamma function.[16] The p-value is the probability that a value of χ^2 smaller than the one observed should occur by accident, due to the statistical errors on the measurements with variance σ^2. A model has therefore to be rejected on statistical grounds if its p-value is close to one. A commonly accepted procedure, which we also use here, consists in rejecting a model if its p-value is larger than 0.9.

The procedure is illustrated in Figs. S13 to S19 for the parameters derived from the

WAXS and SAXS

- Figure S13, lattice contraction. In mild ageing conditions, the constant and linear models both have to be rejected ($p \simeq 1$) so that the slope-and-plateau model is retained. In harsh conditions the constant model has to be rejected, but there is no statistical reason to use a model more complex than the linear ($p = 0.715$).

- Figure S14, crystallite size. Based on strictly statistical grounds, there would be no reason to use a model more complex than the constant ($p = 0.674$ and $p = 0.681$ in mild and harsh conditions). This means that the observed increase of d_{XRD} in harsh conditions is not statistically significant. However, because such a trend is expected on physicochemical grounds, the linear model is retained for d_{XRD} in harsh conditions.

- Figure S15, microstrain. Both in mild and harsh conditions, the constant model has to be rejected, but not the linear model ($p = 0.690$ and $p = 0.712$).

- Figure S16, inner diameter. In mild ageing conditions, the constant and linear models both have to be rejected ($p \simeq 1$) so that the slope-and-plateau model is retained. In harsh conditions the constant model has to be rejected, but there is no statistical reason to use a model more complex than the linear $p \leq 0.9$.

- Figure S17, external diameter. Both in mild and harsh conditions, there is no reason to use a model more complex than the constant ($p = 0.620$ and $p = 0.601$).

- Figure S18, platinum surface area. In mild ageing conditions, the constant and linear models both have to be rejected ($p \geq 0.9$) so that the slope-and-plateau model is retained. In harsh conditions the constant model ($p = 0.761$) is statistically sufficient. Physically, however, that model would be misleading because a very fast decrease of S_{Pt} necessarily takes place. The slope-and-plateau models are therefore retained for both mild and harsh ageing.

- Figure S19, shape parameter of the size distribution. In mild ageing conditions, the constant and linear models both have to be rejected ($p \geq 0.9$) so that the slope-and-plateau model is retained. In harsh conditions, the situation is the same as for S_{Pt}, with $p = 0.871$ for the constant model. We retained the slope-and-plateau model in both conditions because the apparent constancy of k merely means that its decrease was very fast.

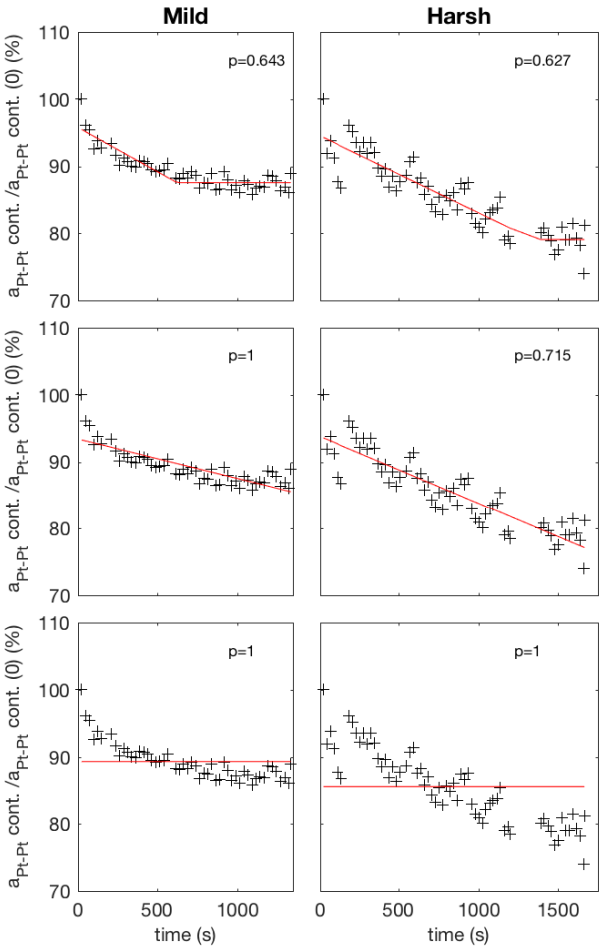

Figure S13: Systematic least-square fitting of the time-dependence of the lattice contraction (same data as in Fig. 3 A of the main text), with the constant (bottom, Eq. S31), linear (middle, Eq. S32) and saturating (top, Eq. S33) models. The mild and harsh ageing conditions are plotted on the left and right, respectively. In each graph, the dots are the values obtained from the WAXS and the red lines are the fits. The p-value of the χ^2 test is also provided.

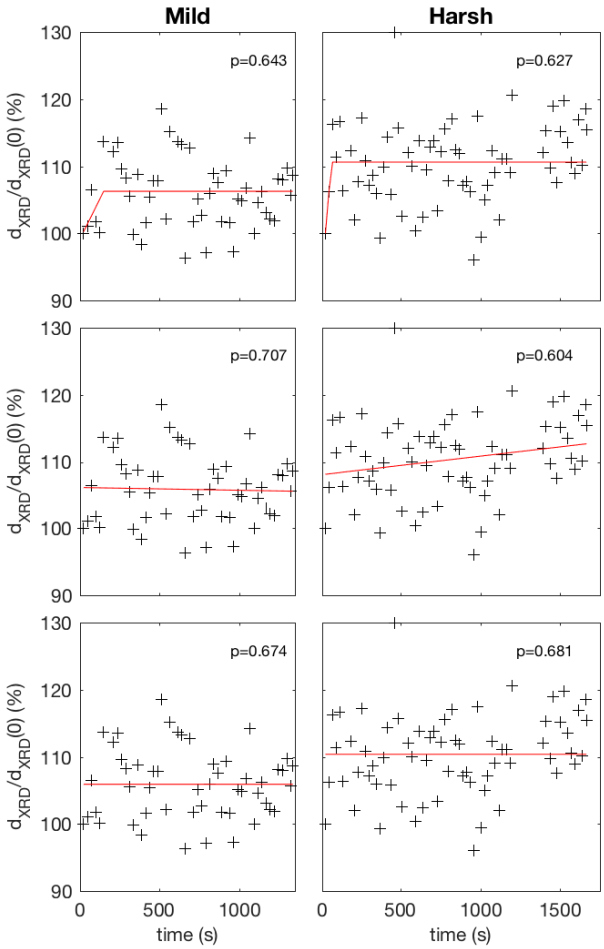

Figure S14: Systematic least-square fitting of the time-dependence of the crystallite size (same data as in Fig. 3 B of the main text), with the constant (bottom, Eq. S31), linear (middle, Eq. S32) and saturating (top, Eq. S33) models. The mild and harsh ageing conditions are plotted on the left and right, respectively. In each graph, the dots are the values obtained from the WAXS and the red lines are the fits. The p-value of the χ^2 test is also provided.

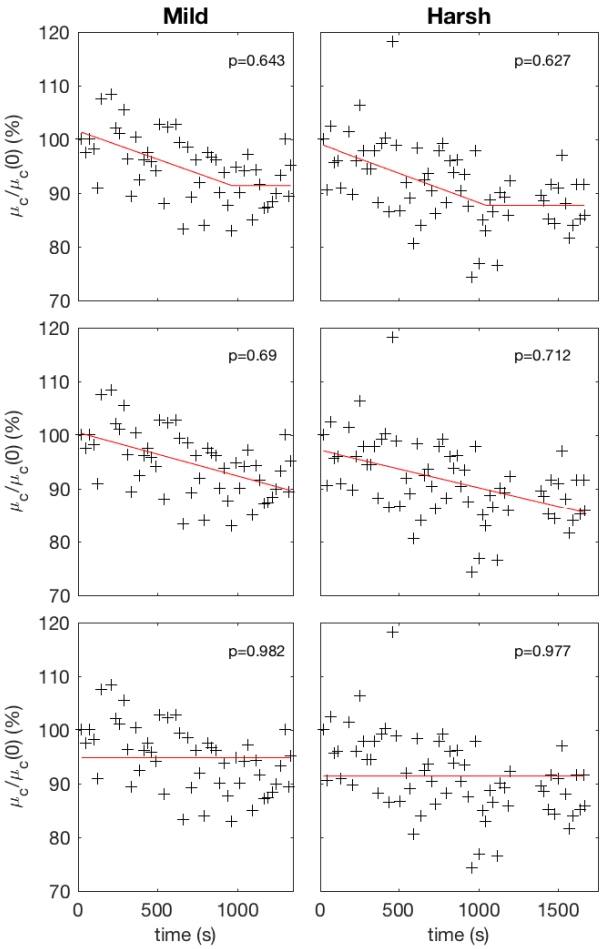

Figure S15: Systematic least-square fitting of the time-dependence of the microstrain (same data as in Fig. 3 C of the main text), with the constant (bottom, Eq. S31), linear (middle, Eq. S32) and saturating (top, Eq. S33) models. The mild and harsh ageing conditions are plotted on the left and right, respectively. In each graph, the dots are the values obtained from the WAXS and the red lines are the fits. The p-value of the χ^2 test is also provided.

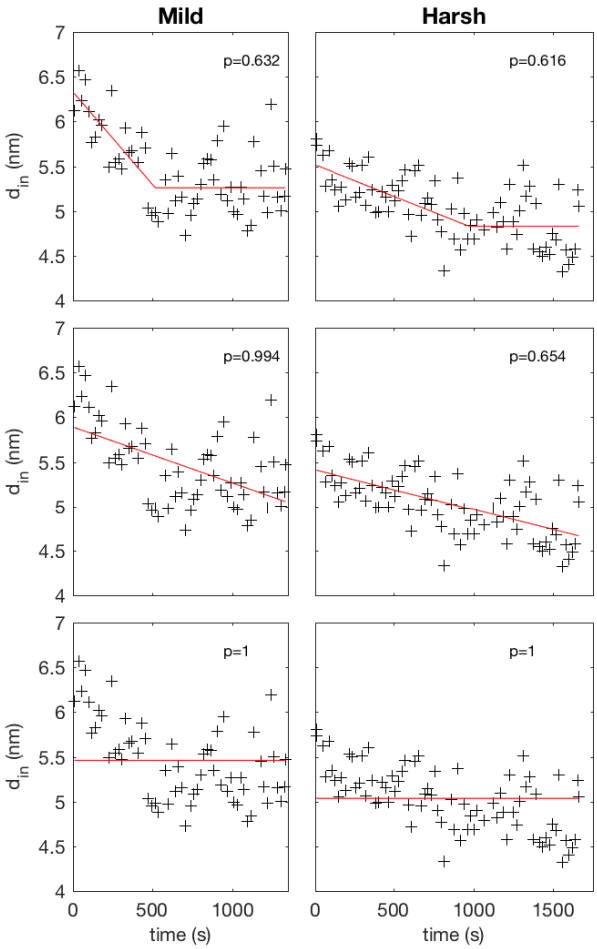

Figure S16: Systematic least-square fitting of the time-dependence of the inner diameter d_{in} of the particles (same data as in Fig. 3 D of the main text), with the constant (bottom, Eq. S31), linear (middle, Eq. S32) and saturating (top, Eq. S33) models. The mild and harsh ageing conditions are plotted on the left and right, respectively. In each graph, the dots are the values obtained from the SAXS and the red lines are the fits. The p-value of the χ^2 test is also provided.

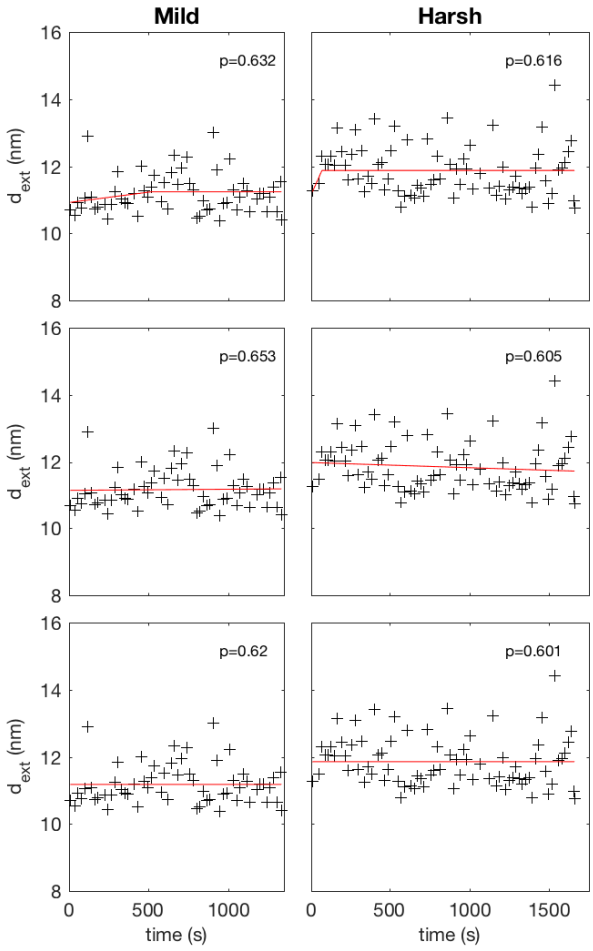

Figure S17: Systematic least-square fitting of the time-dependence of the external diameter d_{ext} of the particles (same data as in Fig. 3 D of the main text), with the constant (bottom, Eq. S31), linear (middle, Eq. S32) and saturating (top, Eq. S33) models. The mild and harsh ageing conditions are plotted on the left and right, respectively. In each graph, the dots are the values obtained from the SAXS and the red lines are the fits. The p-value of the χ^2 test is also provided.

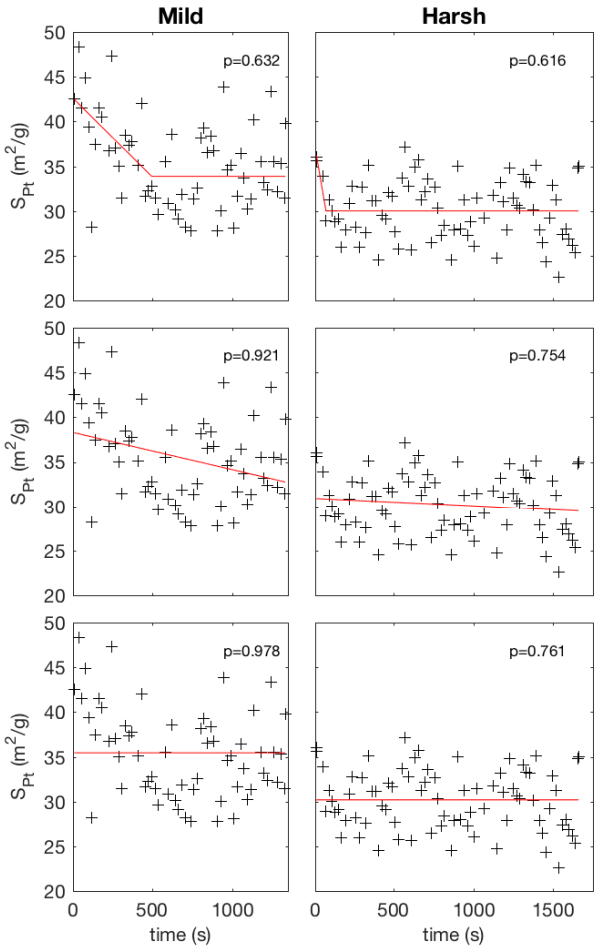

Figure S18: Systematic least-square fitting of the time-dependence of the platinum surface area S_{Pt} (same data as in Fig. 3 E of the main text), with the constant (bottom, Eq. S31), linear (middle, Eq. S32) and saturating (top, Eq. S33) models. The mild and harsh ageing conditions are plotted on the left and right, respectively. In each graph, the dots are the values obtained from the SAXS and the red lines are the fits. The p-value of the χ^2 test is also provided.

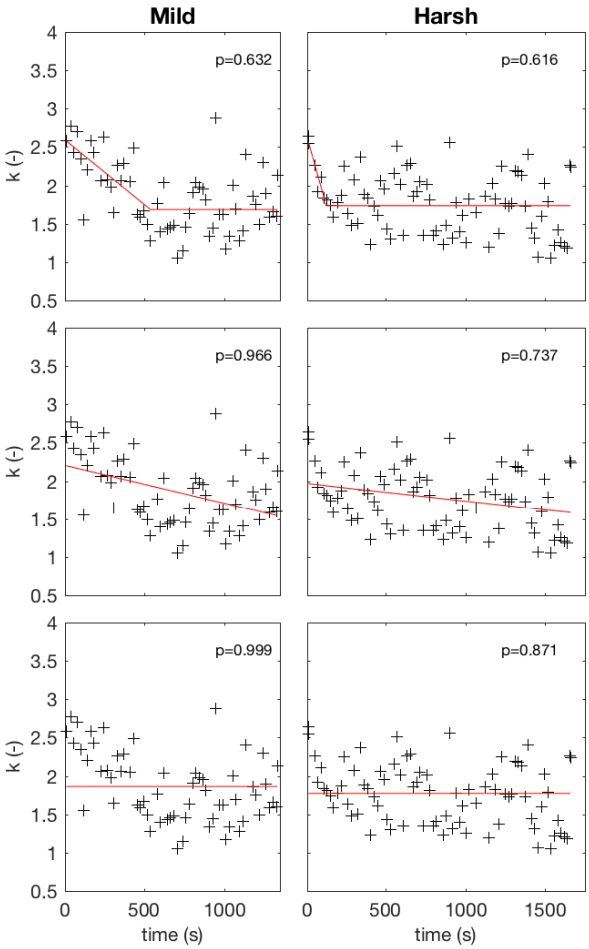

Figure S19: Systematic least-square fitting of the time-dependence of the shape parameter k of the particle size distribution (same data as in Fig. 3 F of the main text), with the constant (bottom, Eq. S31), linear (middle, Eq. S32) and saturating (top, Eq. S33) models. The mild and harsh ageing conditions are plotted on the left and right, respectively. In each graph, the dots are the values obtained from the SAXS and the red lines are the fits. The p-value of the χ^2 test is also provided.

References

(1) Rodrigues Castanheira, L. F. Corrosion of High Surface Area Carbon Supports used in Proton Exchange Membrane Fuel Cell Electrodes. Ph.D. thesis, Université de Grenoble, 2014.

(2) Garsany, Y.; Baturina, O. A.; Swider-Lyons, K. E.; Kocha, S. S. Experimental Methods for Quantifying the Activity of Platinum Electrocatalysts for the Oxygen Reduction Reaction. *Anal. Chem.* **2010**, *82*, 6321–6328.

(3) Garsany, Y.; Singer, I. L.; Swider-Lyons, K. E. Impact of Film Drying Procedures on RDE Characterization of Pt/VC Electrocatalysts. *J. Electroanal. Chem.* **2011**, *662*, 396–406.

(4) Napporn, T. W.; Dubau, L.; Morais, C.; Camilo, M. R.; Durst, J.; Lima, F. H. B.; Maillard, F.; Kokoh, B. In *In situ Characterization Techniques for Nanomaterials*; Kumar, C., Ed.; Springer: Berlin, Heidelberg, 2018; pp 383–439, DOI: 10.1007/978-3-662-56322-9_11.

(5) Ashiotis, G.; Deschildre, A.; Nawaz, Z.; Wright, J. P.; Karkoulis, D.; Picca, F. E.; Kieffer, J. The Fast Azimuthal Integration Python Library: PyFAI. *J. Appl. Crystallogr.* **2015**, *48*, 510–519.

(6) Gommes, C. J.; Prieto, G.; De Jongh, P. E. Small-Angle Scattering Analysis of Empty or Loaded Hierarchical Porous Materials. *J. Phys. Chem. C* **2016**, *120*, 1488–1506.

(7) Guinier, A.; Fournet, G. *Small-Angle Scattering of X-Rays*; Wiley: New York, 1955.

(8) Sivia, D. S. *Elementary Scattering Theory*; Oxford University Press: Oxford, 2011.

(9) Debye, P.; Bueche, A. Scattering by an Inhomogeneous Solid. *J. Appl. Phys.* **1949**, *20*, 518–525.

(10) Perret, R.; Ruland, W. X-Ray Small-Angle Scattering of Non-Graphitizable Carbons. *J. Appl. Cryst.* **1968**, *1*, 308–313.

(11) Perret, R.; Ruland, W. Small-Angle Scattering of Two-Phase Systems: Determination and Significance of Systematic Deviations from Porod's law. *J. Appl. Cryst.* **1968**, *4*, 70–73.

(12) Cohaut, N.; Blanche, C.; Dumas, D.; Guet, J. M.; Rouzaud, J. N. Small-Angle X-ray Scattering Study on the Porosity of Anthracites. *Carbon* **2000**, *38*, 1391–1400.

(13) Gommes, C. J. Stochastic Models of Disordered Mesoporous Materials for Small-Angle Scattering Analysis and More. *Microp. Mesop. Mater.* **2018**, *257*, 62–78.

(14) Gommes, C. J.; Roberts, A. P. Structure Development of Resorcinol-Formaldehyde Gels: Microphase Separation or Colloid Aggregation. *Phys. Rev. E* **2008**, *77*.

(15) Pedersen, J. S. Analysis of Small-Angle Scattering Data from Colloids and Polymer solutions: Modeling and Least-Squares Fitting. *Adv. Coll. Interf. Sci.* **1997**, *70*, 171–210.

(16) Press, W. H.; Teukolsky, S. A.; Vetterling, W. T.; Flannery, B. P. *Numerical Recipes: The Art of Scientific Computing*, 3rd ed.; Cambridge University Press, 2007.